Available online at www.sciencedirect.com
ScienceDirect
Engineering Fracture Mechanics xxx (2006) xxx–xxx
Engineering Fracture Mechanics
www.elsevier.com/locate/engfracmech

Methods for calculating stress intensity factors in anisotropic materials: Part II—Arbitrary geometry

Leslie Banks-Sills [a,b,*], Paul A. Wawrzynek [b], Bruce Carter [b], Anthony R. Ingraffea [b], Itai Hershkovitz [a]

[a] The Dreszer Fracture Mechanics Laboratory, Department of Solid Mechanics, Materials and Systems, The Fleischman Faculty of Engineering, Tel Aviv University, 69978 Ramat Aviv, Israel
[b] School of Civil and Environmental Engineering, Cornell University, Ithaca, 14853 NY, USA

Received 15 February 2006; received in revised form 25 June 2006; accepted 17 July 2006

Abstract

The problem of a crack in a general anisotropic material under conditions of linear elastic fracture mechanics (LEFM) is examined. In Part I, three methods were presented for calculating stress intensity factors for various anisotropic materials in which $z = 0$ is a symmetry plane and the crack front is along the z-axis. These included displacement extrapolation, the M-integral and the separated J-integrals.

In this study, general material anisotropy is considered in which the material and crack coordinates may be at arbitrary angles. A three-dimensional treatment is required for this situation in which there may be two or three modes present. A three-dimensional M-integral is extended to obtain stress intensity factors. It is applied to several test problems, in which excellent results are obtained. Results are obtained for a Brazilian disk specimen made of isotropic and cubic material. Two examples for the latter are examined with material coordinates rotated with respect to the crack axes.

Keywords: Stress intensity factors; Anisotropic material; Finite element method; Three-dimensional M-integral

1. Introduction

In part I of this study [1], the problem of a crack in an anisotropic material was studied for the case in which $x_3 = z = 0$ is a plane of material symmetry. The crack coordinates were defined as x, y and z; whereas, the material coordinates were x_i, $i = 1, 2, 3$ (see Fig. 1).

* Corresponding author. Tel.: +972 3 640 8132; fax: +972 3 640 7617. Address: The Dreszer Fracture Mechanics Laboratory, Department of Solid Mechanics, Materials and Systems, The Fleischman Faculty of Engineering, Tel Aviv University, 69978 Ramat Aviv, Israel.
E-mail addresses: banks@eng.tau.ac.il (L. Banks-Sills), wash@fac.cfg.cornell.edu (P.A. Wawrzynek), bruce@fac.cfg.cornell.edu (B. Carter), ari1@cornell.edu (A.R. Ingraffea), hersh@eng.tau.ac.il (I. Hershkovitz).

0013-7944/$ - see front matter © 2006 Published by Elsevier Ltd.
doi:10.1016/j.engfracmech.2006.07.005

Nomenclature

$\ell_x^{(N)}(z)$ virtual crack extension in the x-direction (see Fig. 2)
m_{ij} defined in general in Eqs. (17)–(19)
n_x normal to the crack front (see Fig. 2)
p_i, $i = 1,2,3$ eigenvalues of the compatibility equations with positive imaginary part
q_i virtual crack extension
r radial crack tip coordinate
t_{ij} matrix of direction cosines between the material and crack tip coordinate systems
u_i, $i = x,y,z$ displacement vector with reference to the crack tip coordinate system
x_i, $i = 1,2,3$ material coordinate system
x, y, z local crack tip coordinate system
A_x area of the virtual crack extension in the plane ahead of the crack (see Eq. (35))
$\widehat{\mathbf{C}}$ contracted stiffness matrix in the material coordinates
$\mathscr{G}(z)$ energy release rate along the crack front
$\Im$ and $\Re$ represent the imaginary and real parts of a complex quantity, respectively
K_j, $j = \mathrm{I,II,III}$ stress intensity factors
L_N length of an element along the crack front (see Fig. 2)
$M^{(1,2\alpha)}$ M-integral with 1 the desired solution and 2α, $\alpha = a,b,c$ the auxiliary solution
N element number along the crack front (see Fig. 2)
N_{ij} 3×3 matrix in Eq. (14)
N_{ij}^{-1} inverse matrix of N_{ij}
Q_i defined in Eq. (13)
R_s 6×6 matrix for rotating the contracted compliance matrix
R_c 6×6 matrix for rotating the contracted stiffness matrix
S_{ij}, $i,j = 1,\ldots,6$ contracted compliance matrix
S'_{ij} reduced compliance matrix (see Eq. (7))
$\widehat{\mathbf{S}}$ contracted compliance matrix in the material coordinates
V volume within which the conservative integral is calculated (see Fig. 2)
W strain energy density
$W^{(1,2\alpha)}$ the interaction strain energy density defined in Eq. (36)
δ_{ij} Kronecker delta
ϵ_{ij}, $i,j = x,y,z$ strain tensor
λ_i defined in Eq. (16)
σ_{xx}, σ_{yy}, σ_{xy}, σ_{zx}, σ_{zy} stress components with reference to the crack tip coordinate system
θ polar crack tip coordinate
θ_x, θ_y, θ_z Euler angles, defined before Eq. (45)

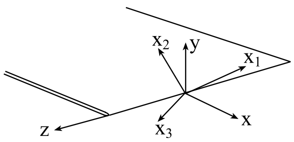

Fig. 1. Crack tip coordinates.

The first term of the asymptotic expressions for the stress and displacement fields for anisotropies in which $z = x_3 = 0$ is a symmetry plane were used in the derivation of three methods for calculating stress intensity factors: displacement extrapolation, M-integral and separated J-integrals. It was shown that the energy based conservation integrals were most accurate. The separated J-integrals were only valid for particular symmetries. Hence, they may not be employed in this part of the investigation.

Instead, the M-integral is extended for the general anisotropic case and presented in Section 2. In Section 3, some numerical examples are described. First, three benchmark problems are considered in which the material is taken to be isotropic and cubic. The material axes for the cubic material are taken to be aligned and rotated with respect to the crack axes. The exact displacement field is used in the context of the finite element method to assess numerical error. Various virtual crack extensions are explored. It is seen that the M-integral produces accurate results. Next, a thick plate containing a central crack is analyzed for various relative positions of a cubic material. Finally, the Brazilian disk specimen also composed of isotropic and cubic material, containing a central crack rotated with respect to the loading axis is discussed.

To begin with, the first term of the asymptotic expressions for the stress and displacement fields originally derived by Hoenig [2] are presented. They are given by

$$\sigma_{xx} = \frac{1}{\sqrt{2\pi r}} \Re\left[\sum_{i=1}^{3} \frac{p_i^2 N_{ij}^{-1} K_j}{Q_i}\right], \tag{1}$$

$$\sigma_{yy} = \frac{1}{\sqrt{2\pi r}} \Re\left[\sum_{i=1}^{3} \frac{N_{ij}^{-1} K_j}{Q_i}\right], \tag{2}$$

$$\sigma_{xy} = -\frac{1}{\sqrt{2\pi r}} \Re\left[\sum_{i=1}^{3} \frac{p_i N_{ij}^{-1} K_j}{Q_i}\right], \tag{3}$$

$$\sigma_{zx} = \frac{1}{\sqrt{2\pi r}} \Re\left[\sum_{i=1}^{3} \frac{p_i \lambda_i N_{ij}^{-1} K_j}{Q_i}\right], \tag{4}$$

$$\sigma_{zy} = -\frac{1}{\sqrt{2\pi r}} \Re\left[\sum_{i=1}^{3} \frac{\lambda_i N_{ij}^{-1} K_j}{Q_i}\right], \tag{5}$$

$$u_i = \sqrt{\frac{2r}{\pi}} \Re\left[\sum_{j=1}^{3} m_{ij} N_{jl}^{-1} K_l Q_j\right], \tag{6}$$

where $\Re$ represents the real part of the quantity in brackets, two repeated indices in Eqs. (1)–(6) obey the summation convention from 1 to 3, the coordinates x, y, and z refer to the crack coordinates in Fig. 1, r and θ are polar coordinates in the $x-y$ plane, K_j represents the stress intensity factors K_I, K_{II} and K_{III}. The contracted compliance matrix S_{ij} is rotated to the crack tip coordinate frame. The indices that relate the tensor and vector forms of the stresses and strains and the full and contracted versions of the stiffnesses and compliances are taken such that $11 \to 1$, $22 \to 2$, $33 \to 3$, $23 \to 4$, $13 \to 5$ and $12 \to 6$. Plane deformation is assumed, so that $\epsilon_{zz} = 0$ to first order; as a result, the reduced compliance matrix is used in the analysis. The components are given by

$$S'_{ij} = S_{ij} - \frac{S_{i3} S_{3j}}{S_{33}}, \tag{7}$$

where $i, j = 1, 2, 4, 5, 6$, S'_{ij} is symmetric and

$$S'_{i3} = S'_{3i} = 0. \tag{8}$$

The parameters p_i, $i = 1$, 2, 3, are the eigenvalues of the compatibility equations with positive imaginary part. These are found, in general, from the characteristic sixth order polynomial equation

$$l_4(p) l_2(p) - l_3^2(p) = 0, \tag{9}$$

where

$$l_2(p) = S'_{55} p^2 - 2S'_{45} p + S'_{44}, \tag{10}$$

$$l_3(p) = S'_{15} p^3 - (S'_{14} + S'_{56}) p^2 + (S'_{25} + S'_{46}) p - S_{24}, \tag{11}$$

$$l_4(p) = S'_{11} p^4 - 2S'_{16} p^3 + (2S'_{12} + S'_{66}) p^2 - 2S'_{26} p + S'_{22}. \tag{12}$$

The expression Q_i is given by

$$Q_i = \sqrt{\cos\theta + p_i \sin\theta}. \tag{13}$$

The matrix

$$N_{ij} = \begin{pmatrix} 1 & 1 & 1 \\ -p_1 & -p_2 & -p_3 \\ -\lambda_1 & -\lambda_2 & -\lambda_3 \end{pmatrix}, \tag{14}$$

its inverse is given by

$$N_{ij}^{-1} = \frac{1}{|N|} \begin{pmatrix} p_2\lambda_3 - p_3\lambda_2 & \lambda_3 - \lambda_2 & p_2 - p_3 \\ p_3\lambda_1 - p_1\lambda_3 & \lambda_1 - \lambda_3 & p_3 - p_1 \\ p_1\lambda_2 - p_2\lambda_1 & \lambda_2 - \lambda_1 & p_1 - p_2 \end{pmatrix}. \tag{15}$$

The parameters λ_i are given by

$$\lambda_i = -\frac{l_3(p_i)}{l_2(p_i)}, \tag{16}$$

where $i = 1, 2, 3$. The parameters m_{ij} in Eq. (6) are given by

$$m_{1i} = S'_{11}p_i^2 - S'_{16}p_i + S'_{12} + \lambda_i(S'_{15}p_i - S'_{14}), \tag{17}$$
$$m_{2i} = S'_{21}p_i - S'_{26} + S'_{22}/p_i + \lambda_i(S'_{25} - S'_{24}/p_i), \tag{18}$$
$$m_{3i} = S'_{41}p_i - S'_{46} + S'_{42}/p_i + \lambda_i(S'_{45} - S'_{44}/p_i). \tag{19}$$

It may be noted that the expressions in (16)–(19) appear to rely on the Lekhnitskii formalism [3], although there are differences with Lekhnitskii for λ_3 and m_{3i}. These expressions developed in [2] are correct.

2. The *M*-integral for calculating stress intensity factors

In this section, a three-dimensional *M*-integral is derived for calculating stress intensity factors of a straight through crack in a body composed of general anisotropic materials. The conservative *M*-integral was first presented in [4] for mixed-mode problems in isotropic material and in [5] for anisotropic materials in which $x_3 = z = 0$ is a symmetry plane.

Here, the crack is at an arbitrary angle to the material axes of a general anisotropic material. As mentioned earlier, crack coordinates are defined as x, y and z as shown in Fig. 1; the x-axis is in the plane of the crack and perpendicular to the crack front, the y-axis is perpendicular to the crack plane and the z-axis is along the crack front. The material coordinates are given by x_i ($i = 1, 2, 3$). The compliance matrix S_{ij} is rotated to coincide with crack coordinates when used in the expressions for the stress and displacement fields in Eqs. (1)–(6).

For this geometry and material, a three-dimensional treatment is required. The three-dimensional *J*-integral was first derived in [6] with another derivation presented in [7]. It may be written as

$$\int_0^{L_N} \mathcal{G}(z)\ell_x^{(N)}(z)n_x \mathrm{d}z = \int_V \left[\sigma_{ij}\frac{\partial u_i}{\partial x_1} - W\delta_{1j}\right]\frac{\partial q_1}{\partial x_j}\mathrm{d}V, \tag{20}$$

where $\mathcal{G}$ is the energy release rate along the crack front, $\delta\ell = \ell_x^{(N)} n_x$ is the normalized virtual crack extension orthogonal to the crack front, n_x is the unit normal to the crack front in the x-direction, N represents element N along the crack front, and L_N is its length (see Fig. 2a). Indicial notation is used on the right hand side of Eq. (20). The strain energy density $W = 1/2\sigma_{ij}\epsilon_{ij}$ and δ_{ij} is the Kronecker delta. The subscripts i and j are used to represent x, y and z; that is, σ_{ij}, ϵ_{ij} and u_i represent the stress, strain and displacement components written in the crack tip coordinate system. Volume V reaches from the crack tip to an arbitrary outer surface S, as illustrated in Fig. 2b. On S, q_1 is zero; it takes on the value ℓ_x along the crack front and is continuously differentiable in V (for details, see [7]).

Please cite this article as: Leslie Banks-Sills et al., Methods for calculating stress intensity factors in anisotropic ..., Engineering Fracture Mechanics (2006), doi:10.1016/j.engfracmech.2006.07.005

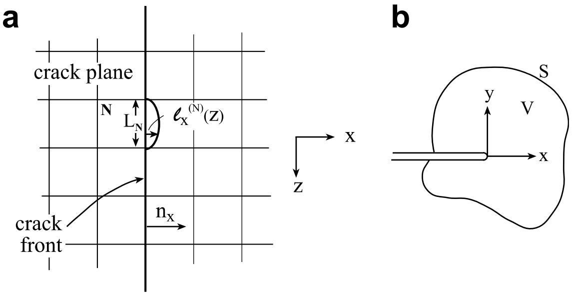

Fig. 2. (a) Virtual crack extension $\delta\ell$ for a through crack denoted on the finite element mesh. (b) In-plane volume V and outer surface S. Note that the integral begins at the crack front.

On the other hand, by means of the crack closure integral, the relationship between the energy release rate and the stress intensity factors may be written as [2]

$$\mathcal{G} = -\frac{1}{2}\{K_{\mathrm{I}}\Im(m_{2i}N_{ij}^{-1}K_j) + K_{\mathrm{II}}\Im(m_{1i}N_{ij}^{-1}K_j) + K_{\mathrm{III}}\Im(m_{3i}N_{ij}^{-1}K_j)\}, \tag{21}$$

where $\Im$ represents the imaginary part of the expression in parentheses and summation should be applied to repeated indices.

The energy release rate $\mathcal{G}$, as well as the stress intensity factors are taken to be piecewise constant along the crack front. The M-integral is calculated within a volume of elements orthogonal to the crack front assuming these unknowns as constant values.

The individual stress intensity factors are obtained from the M-integral. As is usual for this derivation, two equilibrium solutions are superposed; this is possible since the material is linearly elastic. Thus, define

$$\sigma_{ij} = \sigma_{ij}^{(1)} + \sigma_{ij}^{(2)}, \tag{22}$$

$$\epsilon_{ij} = \epsilon_{ij}^{(1)} + \epsilon_{ij}^{(2)}, \tag{23}$$

$$u_i = u_i^{(1)} + u_i^{(2)}. \tag{24}$$

The stress intensity factors associated with the superposed solutions are

$$K_{\mathrm{I}} = K_{\mathrm{I}}^{(1)} + K_{\mathrm{I}}^{(2)}, \tag{25}$$

$$K_{\mathrm{II}} = K_{\mathrm{II}}^{(1)} + K_{\mathrm{II}}^{(2)}, \tag{26}$$

$$K_{\mathrm{III}} = K_{\mathrm{III}}^{(1)} + K_{\mathrm{III}}^{(2)}. \tag{27}$$

Solution (1) is the sought after solution; the fields are obtained by means of a finite element calculation. Solution (2) consists of three auxiliary solutions which are derived from the first term of the asymptotic solution in Eqs. (1)–(6). The stress intensity factors of solutions (2a), (2b) and (2c) are given, respectively, by

$$K_1^{(2a)} = 1, \quad K_{\mathrm{II}}^{(2a)} = 0, \quad K_3^{(2a)} = 0, \tag{28}$$

$$K_1^{(2b)} = 0, \quad K_{\mathrm{II}}^{(2b)} = 1, \quad K_3^{(2b)} = 0 \tag{29}$$

and

$$K_1^{(2c)} = 0, \quad K_{\mathrm{II}}^{(2c)} = 0, \quad K_3^{(2c)} = 1. \tag{30}$$

Substitution of Eqs. (28)–(30) into Eq. (21) with the usual manipulation for the M-integral (see, for example [4,5,8]) leads to

$$M^{(1,2a)} = -\frac{1}{2}\{2K_{\mathrm{I}}^{(1)}\Im(m_{2i}N_{i2}^{-1}) + K_{\mathrm{II}}^{(1)}\Im(m_{1i}N_{i1}^{-1} + m_{2i}N_{i2}^{-1}) + K_{\mathrm{III}}^{(1)}\Im(m_{2i}N_{i3}^{-1} + m_{3i}N_{i1}^{-1})\}, \tag{31}$$

$$M^{(1,2b)} = -\frac{1}{2}\{K_{\mathrm{I}}^{(1)}\Im(m_{2i}N_{i2}^{-1} + m_{1i}N_{i1}^{-1}) + 2K_{\mathrm{II}}^{(1)}\Im(m_{1i}N_{i2}^{-1}) + K_{\mathrm{III}}^{(1)}\Im(m_{1i}N_{i3}^{-1} + m_{3i}N_{i2}^{-1})\}, \tag{32}$$

$$M^{(1,2c)} = -\frac{1}{2}\{K_{\mathrm{I}}^{(1)}\Im(m_{2i}N_{i3}^{-1} + m_{3i}N_{i1}^{-1}) + K_{\mathrm{II}}^{(1)}\Im(m_{1i}N_{i3}^{-1} + m_{3i}N_{i2}^{-1}) + 2K_{\mathrm{III}}^{(1)}\Im(m_{3i}N_{i3}^{-1})\}. \tag{33}$$

Please cite this article as: Leslie Banks-Sills et al., Methods for calculating stress intensity factors in anisotropic ..., Engineering Fracture Mechanics (2006), doi:10.1016/j.engfracmech.2006.07.005

In addition, manipulation of Eq. (20) leads to

$$M^{(1,2\alpha)} = \frac{1}{A_x}\int_V \left[\sigma_{ij}^{(1)}\frac{\partial u_i^{(2\alpha)}}{\partial x_1} + \sigma_{ij}^{(2\alpha)}\frac{\partial u_i^{(1)}}{\partial x_1} - W^{(1,2\alpha)}\delta_{1j}\right]\frac{\partial q_1}{\partial x_j}\mathrm{d}V, \tag{34}$$

where $\alpha = a$, b and c in succession, $n_x = 1$,

$$A_x = \int_0^{L_N} \ell_x^{(N)}(z)\mathrm{d}z, \tag{35}$$

and the interaction energy density

$$W^{(1,2\alpha)} = \sigma_{ij}^{(1)}\epsilon_{ij}^{(2\alpha)} = \sigma_{ij}^{(2\alpha)}\epsilon_{ij}^{(1)}. \tag{36}$$

Values of the stress, strain and displacement fields obtained from a finite element calculation are substituted into Eq. (34) as solution (1), together with each auxiliary solution to compute three values of $M^{(1,2\alpha)}$. Using these values in the left hand sides of Eqs. (31)–(33) leads to three simultaneous equations for K_{I}, K_{II} and K_{III}.

3. Numerical calculations

In this section, results from several calculations are presented. First, three benchmark cases are described in Section 3.1 to examine different virtual crack extensions, as well as to demonstrate the excellent results obtained by means of the M-integral. In these cases, the first term of the asymptotic displacement field with different values for the stress intensity factors is prescribed on one or two elements. In Section 3.2, finite element analyses are carried out on a thick, large plate containing a central crack. Tensile and in-plane shear stresses are imposed separately. Stress intensity factors are computed and compared to plane strain values. Then, in Section 3.3, solutions are presented for a Brazilian disk specimen composed of cubic material rotated with respect to the crack plane and loaded with two different angles. For comparison purposes, an isotropic Brazilian disk specimen is also examined.

The stress intensity factors obtained are average values along the crack front within each element or a pair of elements. Therefore, the results are not continuous through the thickness. In the graphs however, either the mid-point of each element or an element corner is taken as the z-coordinate, so that the curves remain smooth.

In this study, prismatic elements are employed about the crack front as shown in Figs. 3a and b for one or two rings of elements, respectively. The second ring consists of brick elements. The relation between the crack front coordinates and the material coordinates is presented in the Appendix.

For a through crack, two types of virtual crack extensions are examined. The first is the parabolic extension shown in Fig. 4a. This is denoted as $q_1^{(1)}$ and carried out in one layer of elements along the crack front as shown in Fig. 3a or b. The second type of virtual crack extension is shown in Fig. 4b. This is denoted as $q_1^{(2)}$ and carried out in two element layers along the crack front. At the surface of the body, two other virtual crack extensions may be considered. At the front and back surfaces of the body, the virtual crack extensions are illustrated, respectively, in Figs. 4c and d, and denoted as $q_1^{(3)}$ and $q_1^{(4)}$. Each is carried out in one layer of elements.

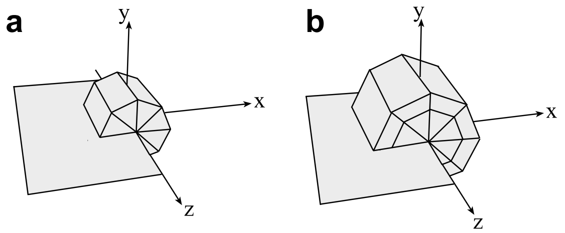

Fig. 3. Domain of integration using (a) one or (b) two rings of elements.

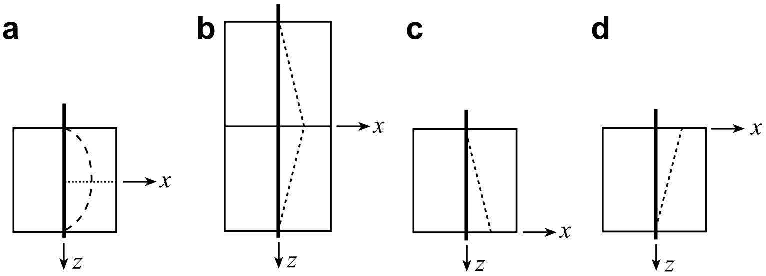

Fig. 4. Virtual crack extensions: (a) parabolic denoted $q_1^{(1)}$, (b) linear (two-sided), $q_1^{(2)}$ (c) linear (front surface), $q_1^{(3)}$, and (d) linear (back surface), $q_1^{(4)}$.

3.1. Prescribed displacement tests

An initial series of tests are performed to verify implementation of the M-integral. In these tests, finite element analyses are not carried out. Rather, nodal displacements for all elements participating in the M-integral evaluation are determined from Eq. (6). Three cases are considered in which one of the stress intensity factors is assumed unity and the other two are assumed zero. The displacements are used to determine the stress and strain components by means of a finite element formulation and substituted into Eq. (34) for the M-integral. The stress intensity factors found by solving Eqs. (31)–(33) simultaneously are compared to the prescribed values.

The purpose of these tests is two-fold. First, as verification; if the M-integral evaluation is encoded correctly, then the computed stress intensity factors should be close to the prescribed values. Second, the difference between the prescribed and computed values gives a quantitative assessment of the ‘intrinsic’ error in the computations and an indication of the relative performance of the differing q_1 functions and the number of element rings. Intrinsic errors are those which arise from the approximate numerical techniques used to calculate the integrals.

Three material types are considered: isotropic, cubic with $x_3 = z = 0$ a symmetry plane, and general anisotropic. The stress intensity factors obtained for isotropic material do not depend upon material properties. The cubic material chosen for study is used in jet engine turbine blades. It is a single crystal, nickel-based superalloy (PWA 1480/1493) described in a NASA report [9]. The material properties are presented in Table 1.

Results are presented in Table 2 for isotropic material and the four crack extensions and one or two rings. It may be observed for the $K_I = 1$ case that the two other stress intensity factors are zero when either one or two

Table 1
Cubic mechanical properties for PWA 1480/1493 [9]

$E_{11} = E_{22} = E_{33} = 15.4 \times 10^6$ (psi)
$\mu_{12} = \mu_{23} = \mu_{13} = 15.7 \times 10^6$ (psi)
$\nu_{12} = \nu_{23} = \nu_{13} = 0.4009$

Table 2
Computed stress intensity factors for prescribed nodal displacements: isotropic material

Rings	$q_1^{(n)}$	Prescribed $K_I = 1$			Prescribed $K_{II} = 1$			Prescribed $K_{III} = 1$		
	n	K_I	K_{II}	K_{III}	K_I	K_{II}	K_{III}	K_I	K_{II}	K_{III}
1	1	0.969	10^{-17}	10^{-17}	10^{-16}	0.970	10^{-17}	10^{-18}	10^{-18}	0.956
	2	1.011	10^{-17}	10^{-19}	10^{-17}	1.005	10^{-18}	10^{-18}	10^{-18}	1.007
	3	1.011	10^{-18}	0	10^{-17}	1.005	0.054	10^{-18}	0.085	1.007
	4	1.011	10^{-17}	10^{-18}	10^{-17}	1.005	−0.054	10^{-18}	−0.085	1.007
2	1	0.997	10^{-16}	10^{-17}	10^{-16}	0.999	10^{-17}	10^{-17}	10^{-18}	0.999
	2	0.997	10^{-18}	0	10^{-17}	0.999	10^{-18}	10^{-18}	10^{-18}	0.999
	3	0.997	10^{-17}	10^{-17}	10^{-17}	0.999	0.153	10^{-17}	0.251	0.999
	4	0.997	10^{-17}	10^{-17}	10^{-17}	0.999	−0.153	10^{-17}	−0.251	0.999

Please cite this article as: Leslie Banks-Sills et al., Methods for calculating stress intensity factors in anisotropic ..., Engineering Fracture Mechanics (2006), doi:10.1016/j.engfracmech.2006.07.005

rings are used in the integration scheme with any of the virtual crack extensions. With two rings, all of the stress intensity factors which are prescribed to be unity converge to the same value near unity for each of the virtual crack extensions. However, the mode two and three stress intensity factors K_{II} and K_{III} are not zero, respectively, when K_{III} and K_{II} are prescribed to be unity and the crack extension is given in either Figs. 4c or d. That is, the non-symmetric virtual crack extension for the front and back surfaces of the body, do not lead to the correct results. It may also be noted that the parabolic virtual crack extension in Fig. 4a leads to less accurate results when integrating in one ring only.

For the cubic material in which the material and crack axes coincide, results are exhibited in Table 3. The behavior obtained for the cubic material is identical to that obtained for the isotropic material. When the virtual crack extension $q_1^{(1)}$ is employed with one integration ring, the results for the dominant stress intensity factor deteriorates in comparison to those for the other virtual crack extensions. For two integration rings, the results for the dominant stress intensity factors are identical for all virtual crack extensions to many more significant figures than shown. They are also more accurate as compared to that obtained with one integration ring. For the stress intensity factors which are prescribed to be zero, $q_1^{(3)}$ and $q_1^{(4)}$ provide results which are not as close to zero as those found with the other two crack extensions. Interestingly, they are opposite in sign; so that when $q_1^{(2)}$ is used, their sum is obtained which is zero. This may also be observed for the isotropic material in Table 2.

Finally, results for a more general case are shown in Table 4. In this case, the same cubic material whose properties are presented in Table 1 is used. Here however, the material axes do not coincide with the crack axes. To this end, three rotations, given as Euler angles, are used to obtain the compliance matrix in the crack axes. These are $\theta_z = \theta_x = \theta_y = \pi/4$ (see the Appendix for the definition of the Euler angles used in this investigation). The components of the 3×3 matrix of direction cosines are given in Eq. (45). The compliance matrix is full although some of the 21 components are either equal or opposite in sign. Here, it may be observed that again using only one integration ring and the parabolic virtual crack extension leads to the least accurate

Table 3
Computed stress intensity factors for prescribed nodal displacements: cubic material

Rings	$q_1^{(n)}$	Prescribed $K_{\text{I}} = 1$			Prescribed $K_{\text{II}} = 1$			Prescribed $K_{\text{III}} = 1$		
	n	K_{I}	K_{II}	K_{III}	K_{I}	K_{II}	K_{III}	K_{I}	K_{II}	K_{III}
1	1	0.953	10^{-9}	10^{-18}	10^{-8}	0.962	10^{-14}	10^{-18}	10^{-14}	0.954
	2	1.008	10^{-10}	10^{-18}	10^{-8}	1.007	10^{-14}	10^{-19}	10^{-14}	1.007
	3	1.008	10^{-10}	10^{-10}	10^{-8}	1.007	0.003	10^{-9}	0.003	1.007
	4	1.008	10^{-10}	10^{-10}	10^{-8}	1.007	−0.003	10^{-9}	−0.003	1.007
2	1	1.003	10^{-10}	10^{-17}	10^{-8}	1.001	10^{-14}	10^{-18}	10^{-14}	1.000
	2	1.003	10^{-10}	10^{-19}	10^{-8}	1.001	10^{-14}	10^{-19}	10^{-14}	1.000
	3	1.003	10^{-10}	10^{-19}	10^{-8}	1.001	0.006	10^{-9}	0.009	1.000
	4	1.003	10^{-10}	10^{-9}	10^{-8}	1.001	−0.006	10^{-9}	−0.009	1.000

Table 4
Computed stress intensity factors for prescribed nodal displacements: cubic material with $\theta_x = \theta_y = \theta_z = \pi/4$

Rings	$q_1^{(n)}$	Prescribed $K_{\text{I}} = 1$			Prescribed $K_{\text{II}} = 1$			Prescribed $K_{\text{III}} = 1$		
	n	K_{I}	K_{II}	K_{III}	K_{I}	K_{II}	K_{III}	K_{I}	K_{II}	K_{III}
1	1	0.960	0.007	0.001	0.007	0.965	−0.003	0.004	−0.005	0.959
	2	1.009	0.001	10^{-4}	0.001	1.006	10^{-5}	10^{-4}	10^{-4}	1.007
	3	1.007	−0.005	0.002	−0.003	0.993	0.033	−0.011	0.086	1.020
	4	1.012	0.007	−0.002	0.005	1.019	−0.033	0.012	−0.086	0.994
2	1	0.998	−0.005	−0.001	−0.005	0.999	0.002	0.001	0.005	0.999
	2	0.998	−0.005	−0.001	−0.005	0.999	0.001	−0.003	0.004	0.998
	3	0.991	−0.022	0.005	−0.017	0.961	0.096	−0.034	0.259	1.039
	4	1.006	0.011	−0.007	0.007	1.037	−0.093	0.029	−0.252	0.957

Please cite this article as: Leslie Banks-Sills et al., Methods for calculating stress intensity factors in anisotropic ..., Engineering Fracture Mechanics (2006), doi:10.1016/j.engfracmech.2006.07.005

results for the dominant stress intensity factor. With two rings, both the parabolic and double triangular virtual crack extension lead to nearly the same results. For this case, the stress intensity factors which are prescribed to be zero are much less accurate than that for the isotropic and cubic materials. Moreover, there is a further deterioration of these results when obtained with $q_1^{(3)}$ and $q_1^{(4)}$.

From this sample of results, as well as experience with other numerical experiments, the latter two virtual crack extensions are not recommended. It may also be pointed out, that these crack extensions are used only at the surfaces of a body. At that corner point, the character of the singularity changes and a value for the stress intensity factor obtained in this way is not relevant.

3.2. Thick plate analysis

In this section, a thick plate, illustrated in Fig. 5, is considered. Since $W/a = 15$ and $h/W = 1$, the plate can be thought of as being infinite in the x–y plane; the thickness $B/W = 1$. With this thickness, plane strain conditions are approximated in the center of the plate. Boundary conditions to prevent rigid body motion are shown in Fig. 6a. The plate is loaded in tension as shown in Fig. 6b, and in pure in-plane shear as shown in Fig 6c.

The model and meshes were generated with FRANC3D [10]. The finite element analysis was performed with ANSYS [11]. The computed nodal point displacements were read back into FRANC3D where the M-integral was evaluated to determine the stress intensity factors. The virtual crack extensions in Figs. 4a and b were employed using two element rings as shown in Fig. 3b.

The mesh shown in Fig. 7a was used for all analyses. A detail of the crack tip region is illustrated in Fig. 7b. The mesh contains a total of 81,502 elements which are predominantly 10 noded tetrahedral elements. There are 15 noded quarter-point wedge elements around the crack front with two rings of twenty noded brick elements surrounding the crack tip elements. Thirteen noded pyramid elements serve as a transition from the brick elements to tetrahedral elements, as well as to the 20 noded outer bricks in the remainder of the mesh. There are 68 elements through the specimen thickness along the crack front. There is a total of 121,490 nodal points.

Four material cases are examined. In the first case, the material is taken to be isotropic with Young's modulus $E = 15.4 \times 10^6$ psi and Poisson's ratio $\nu = 0.4009$. These are the same values as those for the cubic material. The material properties for a cubic material in Table 1 are used for three other cases. These include:

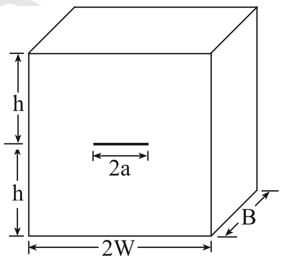

Fig. 5. Thick plate geometry containing a central through crack.

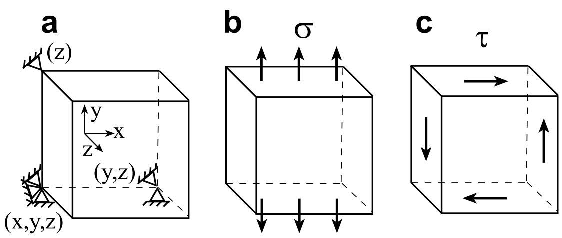

Fig. 6. (a) Simply supported boundary conditions. (b) Applied tensile stress and (c) in-plane shear stress used in the analyses.

Please cite this article as: Leslie Banks-Sills et al., Methods for calculating stress intensity factors in anisotropic ..., Engineering Fracture Mechanics (2006), doi:10.1016/j.engfracmech.2006.07.005

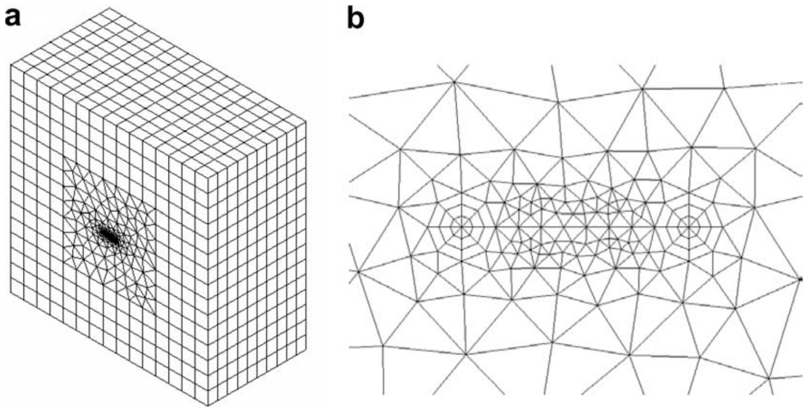

Fig. 7. (a) The mesh used for the thick plate analyses containing 121,490 nodal points. (b) A detail of the thick plate mesh in the crack region.

(1) the material coordinates aligned with the crack axes, (2) $\theta_y = \pi/4$ (the material appears transversely isotropic with the symmetry plane $y = 0$) and (3) $\theta_z = \theta_x = \theta_y = \pi/4$. The latter is the same material used in the previous section where the compliance matrix is full, although there are relations between some of the components. It will be denoted here as triclinic.

Results for applied tension are presented in Fig. 8. The abscissa is the normalized coordinate along the crack front z/B. The values of the stress intensity factors are normalized by the two-dimensional plane strain value for the infinite plate of $K_{\mathrm{I}} = \sigma\sqrt{\pi a}$. It may be observed in Fig. 8a that within the central portion of the plate, the normalized $\widehat{K}_I$ for each case approaches unity. There is a small divergence for the transversely isotropic material ($\theta_y = \pi/4$). Possibly the plate is not sufficiently large to be infinite for this case. For the isotropic plate and the plates with $\theta_y = 0$ and $\theta_y = \pi/4$, the results are symmetric with respect to the center line. As expected, this does not occur for the case in which the material is triclinic in the crack coordinates. Moreover, for the cubic material, $\widehat{K}_{\mathrm{I}}$ reaches the highest values near the specimen surface.

In Fig. 8b, $\widehat{K}_{\mathrm{II}}$ and $\widehat{K}_{\mathrm{III}}$ are plotted for the triclinic material. For the other three materials, these values are essentially zero along the entire crack front. It may be observed that $\widehat{K}_{\mathrm{II}}$ and $\widehat{K}_{\mathrm{III}}$ are not symmetric with respect to the center line of the plate. In addition, $\widehat{K}_{\mathrm{II}}$ rises to about 8.4% of the two-dimensional K_{I} value, whereas $\widehat{K}_{\mathrm{III}}$ rises to about 2.3% of this value. It may be noted that these increases occur over distances of 10% to more than 20% of the plate thickness.

For pure in-plane shear shown in Fig. 6c, normalized stress intensity factors are presented in Fig. 9. The normalizing factor is that for the two-dimensional solution for the same infinite body, namely, $K_{\mathrm{II}} = \tau\sqrt{\pi a}$.

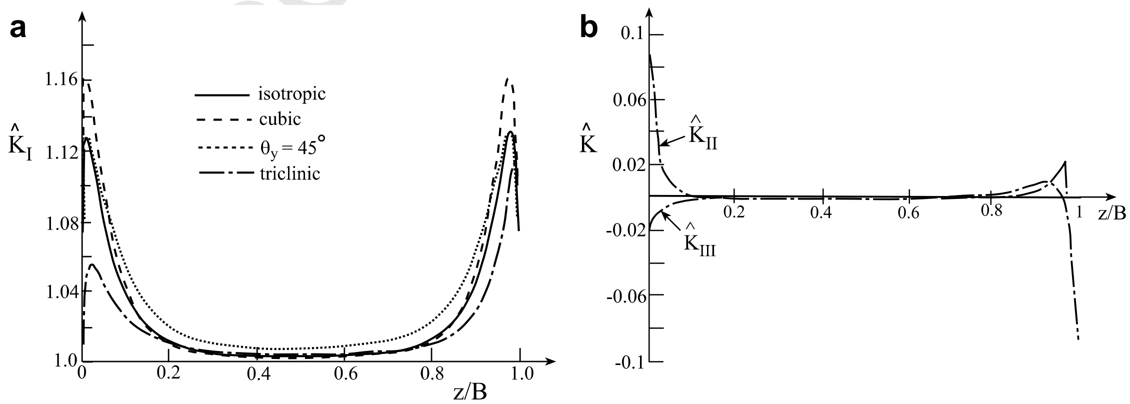

Fig. 8. (a) Values of $\widehat{K}_{\mathrm{I}}$ as a function of plate thickness for the tensile load. (b) Values of $\widehat{K}_{\mathrm{II}}$ and $\widehat{K}_{\mathrm{III}}$ for the triclinic material.

Please cite this article as: Leslie Banks-Sills et al., Methods for calculating stress intensity factors in anisotropic ..., Engineering Fracture Mechanics (2006), doi:10.1016/j.engfracmech.2006.07.005

Interestingly, the values for $\widehat{K}_{\rm II}$ in the center of the plate approach unity for the isotropic and triclinic materials (see Fig. 9a). Symmetry about the center of the plate is achieved for the isotropic, as well as the cubic and transversely isotropic ($\theta_y = \pi/4$) materials. The results for the triclinic material are not symmetric. The surface effects may be noted. In addition, as seen in Fig. 9b, the values of $\widehat{K}_{\rm III}$ are anti-symmetric with respect to the plate centerline for all but the triclinic material. In that case, the values are nearly anti-symmetric. A clear surface effect is observed. Finally, the behavior of $\widehat{K}_{\rm I}$ is not shown. For all but the triclinic material, its value is essentially zero. For the triclinic material, $\widehat{K}_{\rm I}$ rises to above 4% of the plane strain $K_{\rm II}$ value near one surface and oscillates between 1% and −0.5% at the other surface.

3.3. Brazilian disk specimen

The Brazilian disk specimen illustrated in Fig. 10 is studied in this section. The specimen is analyzed for several crack lengths with $0.2 \leqslant a/R \leqslant 0.8$ where $2a$ is crack length and R is the radius of the disk. Three materials are considered: isotropic and two anisotropic cases. For the isotropic material, Young's modulus $E = 1 \times 10^6$ psi and Poisson's ratio $\nu = 0.4$. Of course, for isotropic material and traction boundary conditions, the stress intensity factors do not depend upon mechanical properties. For the two anisotropic cases, the cubic material properties in Table 1 are rotated with respect to the crack axes. In the first, the local crack front axes have the following orientation with respect to the material axes $\langle 1\underline{1}0/1\,1\,1\rangle$ where $\langle x/y\rangle$ are the directions shown in Fig. 10. The matrix of direction cosines is given by

$$t_{ij}^{(1)} = \begin{bmatrix} \frac{1}{\sqrt{2}} & -\frac{1}{\sqrt{2}} & 0 \\ \frac{1}{\sqrt{3}} & \frac{1}{\sqrt{3}} & \frac{1}{\sqrt{3}} \\ -\frac{1}{\sqrt{6}} & -\frac{1}{\sqrt{6}} & \frac{2}{\sqrt{6}} \end{bmatrix}. \tag{37}$$

Using Eq. (45), it is possible to obtain the Euler angles as $\theta_z = 50.7685°$, $\theta_x = -24.0948°$ and $\theta_y = 26.5650°$. In the second case, $\langle x/y\rangle = \langle 1\,1\,\underline{2}/1\,1\,1\rangle$ so that

$$t_{ij}^{(2)} = \begin{bmatrix} \frac{1}{\sqrt{6}} & \frac{1}{\sqrt{6}} & -\frac{2}{\sqrt{6}} \\ \frac{1}{\sqrt{3}} & \frac{1}{\sqrt{3}} & \frac{1}{\sqrt{3}} \\ \frac{1}{\sqrt{2}} & -\frac{1}{\sqrt{2}} & 0 \end{bmatrix}. \tag{38}$$

Here the Euler angles are $\theta_z = -35.2644°$, $\theta_x = -45.0°$ and $\theta_y = -90.0°$.

For isotropic material and the $\langle 1\underline{1}0/1\,1\,1\rangle$ material configuration, the loading angle is taken to be $\theta = 8°$. For these two cases, symmetric results are obtained for positive and negative values of θ. For the cubic material rotated to the crack axes, the material appears monoclinic with $x = 0$ a symmetry plane. For the $\langle 1\,1\,\underline{2}/$

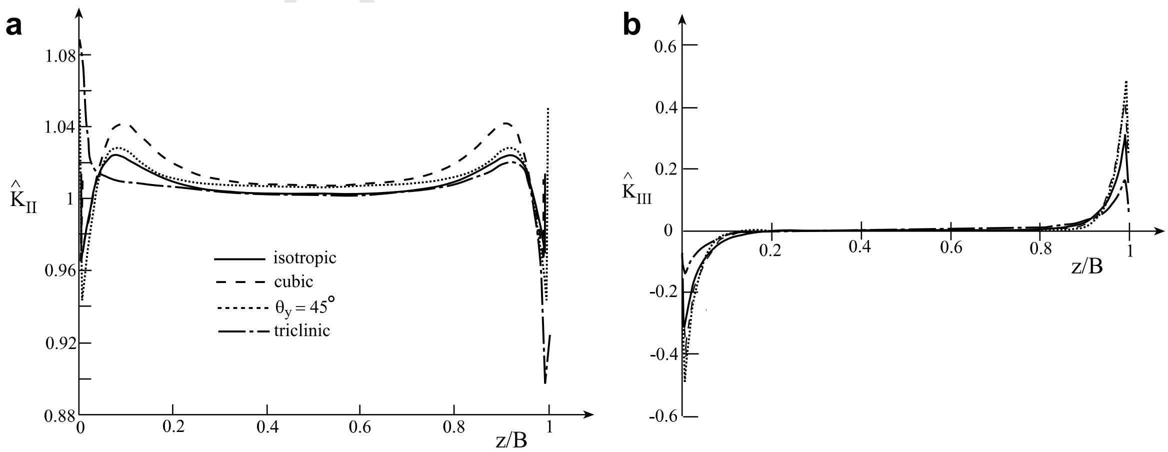

Fig. 9. (a) Values of $\widehat{K}_{\rm II}$ and (b) $\widehat{K}_{\rm III}$ as a function of plate thickness for the in-plane shear load.

Please cite this article as: Leslie Banks-Sills et al., Methods for calculating stress intensity factors in anisotropic ..., Engineering Fracture Mechanics (2006), doi:10.1016/j.engfracmech.2006.07.005

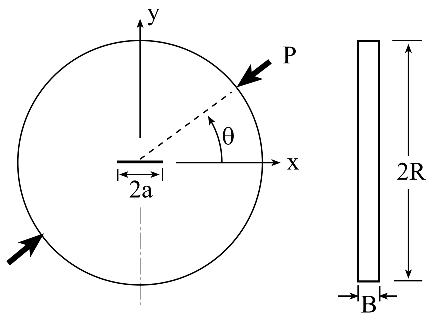

Fig. 10. The geometry of the Brazilian disk specimen.

1 1 1⟩ material configuration, both $\theta = 8°$ and $-8°$ are considered. This material appears to be a monoclinic material with $z = 0$ a plane of symmetry.

A typical mesh used in the analyses is shown in Fig. 11. The meshes contained between 4128 and 5588 isoparametric elements and 15,024–20,558 nodal points, respectively, depending upon crack length. Although three-dimensional behavior was observed at the specimen surfaces for the thick plate, the mesh here contains two elements in the thickness direction with periodic conditions applied to its front and back surfaces to enforce plane strain conditions. The mesh contains predominantly fifteen noded wedge elements, with quarter-point wedge elements at the crack fronts. There is a ring of twenty noded brick elements connected to the quarter-point wedge elements.

The stress intensity factors K_{I}, K_{II} and K_{III} are obtained by means of the M-integral using $q_1^{(2)}$ in Fig. 4b. This yields a value at the center line of the mesh. The stress intensity factors are normalized so that

$$\widehat{K}_{\mathrm{m}} = \frac{K_{\mathrm{m}}}{\sigma\sqrt{\pi a}}, \tag{39}$$

where $m = \mathrm{I}, \mathrm{II}, \mathrm{III}$,

$$\sigma = \frac{P}{\pi R B} \tag{40}$$

and B is specimen thickness.

For the loading angle $\theta = 8°$, results for all material cases are plotted in Fig. 12a. This plot includes the three modes for isotropic material and the two cubic cases. It may be observed that the $\widehat{K}_{\mathrm{I}}$ and $\widehat{K}_{\mathrm{II}}$ values for the three materials are rather similar. The isotropic material leads to the highest values of $\widehat{K}_{\mathrm{I}}$. For the cubic material with directions $\langle 1\,\underline{1}\,0/1\,1\,1\rangle$, the highest absolute values of $\widehat{K}_{\mathrm{II}}$ are obtained. The absolute value of $\widehat{K}_{\mathrm{II}}$ increases monotonically as crack length increases. The mode I stress intensity factor reaches a maximum and

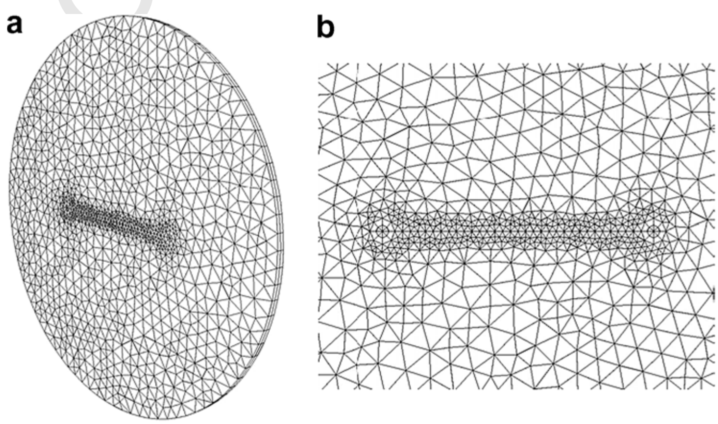

Fig. 11. (a) The mesh used for analyzing the Brazilian disk specimen. (b) Detail surrounding the crack.

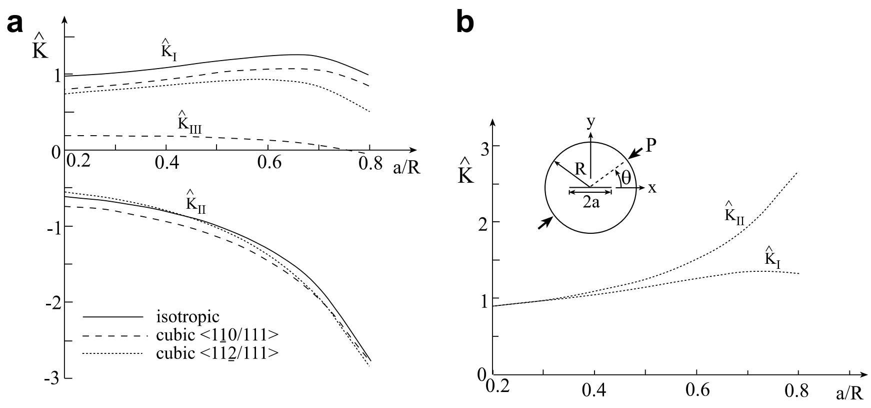

Fig. 12. Values of the normalized stress intensity factors $\widehat{K}$ as a function of normalized crack length a/R for a Brazilian disk specimen (a) made of isotropic and cubic material when $\theta = 8°$ and (b) made of cubic material with $\langle 1\,1\,\underline{2}/1\,1\,1\rangle$ and $\theta = -8°$.

then decreases; at $a/R = 0.8$ its value is less than or equal to its value at $a/R = 0.2$ for each material type. Of course, one must consider a mixed-mode failure criterion to predict failure. Values of $\widehat{K}_{\mathrm{III}}$ are zero for the isotropic material and the cubic material with directions $\langle 1\,1\,\underline{2}/1\,1\,1\rangle$. For those two cases, there is material symmetry with respect to the plane $z = 0$. Of course, this occurs at the center of the specimen. It is expected for the finite thickness specimen, that values of $\widehat{K}_{\mathrm{III}}$ will not be zero away from the centerline. As may be observed in Fig. 12a, the value of $\widehat{K}_{\mathrm{III}}$ is positive for the right crack tip (see Fig. 10) for most values of a/R; for the left crack tip, the opposite sign is obtained. Finally, in Fig. 12b the behavior of the normalized stress intensity factors is completely different for $\langle 1\,1\,\underline{2}/1\,1\,1\rangle$ and $\theta = -8°$. Both $\widehat{K}_{\mathrm{I}}$ and $\widehat{K}_{\mathrm{II}}$ increase with increasing crack length.

4. Summary and conclusions

In this study, a three-dimensional, conservative M-integral is presented for a generally anisotropic body containing a crack. With the M-integral, the stress intensity factors may be obtained separately. To this end, the first term of the asymptotic expansion of the displacement fields determined in [2] for a crack in a general anisotropic material are employed as an auxiliary solution. Finite element analysis are conducted to determine the displacement field of the actual cracked body.

Excellent results were obtained for several benchmark problems by employing the asymptotic displacement field in a finite element formulation. The 'intrinsic' error of the M-integral was seen to be small. Two problems were considered: a thick plate and a Brazilian disk specimen. For the thick plate, results obtained within the specimen were close to that of a two-dimensional solution for both tension and in-plane shear. Edge effects were particularly noticeable for anisotropic material. New results were presented for Brazilian disk specimens of cubic material rotated with respect to the specimen axes. For this case, the surfaces of the specimen were constrained to enforce plane strain conditions. In another study, three-dimensional effects will be examined.

The M-integral is an effective and accurate method for calculating stress intensity factors in mixed-mode situations. It has been extended here to generally anisotropic materials.

Appendix. Relation between crack front, global and material coordinates

The case of orthotropic material properties in the material coordinates x_i is considered. Here, there are nine independent material properties, Young's moduli, E_1, E_2, E_3, Poisson's ratios, ν_{12}, ν_{23}, ν_{13}, and shear moduli, G_{12}, G_{23}, G_{31}. The relation between the Young's moduli and Poisson's ratios is given by

$$\frac{\nu_{ij}}{E_i} = \frac{\nu_{ji}}{E_j}, \tag{41}$$

where there is no summation, and $i, j = 1, 2, 3$.

Please cite this article as: Leslie Banks-Sills et al., Methods for calculating stress intensity factors in anisotropic ..., Engineering Fracture Mechanics (2006), doi:10.1016/j.engfracmech.2006.07.005

The compliance matrix in the material coordinate system is

$$\widehat{\mathbf{S}} = \begin{bmatrix} 1/E_1 & -\nu_{12}/E_1 & -\nu_{13}/E_1 & 0 & 0 & 0 \\ & 1/E_2 & -\nu_{23}/E_3 & 0 & 0 & 0 \\ & & 1/E_3 & 0 & 0 & 0 \\ & & & 1/G_{23} & 0 & 0 \\ & & & 0 & 1/G_{13} & 0 \\ \text{sym} & & & 0 & 0 & 1/G_{12} \end{bmatrix}. \tag{42}$$

The matrix in Eq. (42) may be inverted to yield the stiffness matrix as

$$\widehat{\mathbf{C}} = \widehat{\mathbf{S}}^{-1}. \tag{43}$$

The stiffness and compliance matrices must be rotated to the global finite element coordinate system, as well as the crack tip coordinate system. To this end, the 3×3 matrix of direction cosines $\mathbf{t}$ is defined between the two coordinate systems. There are several ways to carry out this transformation. The finite element community typically uses for the two-dimensional transformation, for example,

$$\beta_{ij} = \begin{bmatrix} \cos\theta & -\sin\theta & 0 \\ \sin\theta & \cos\theta & 0 \\ 0 & 0 & 1 \end{bmatrix}. \tag{44}$$

It may be noted that the elasticity community uses the transform of this matrix (see for example, [12] pp. 28–31 or [13] p. 40, eq. (2.5–6)).

For three dimensions, the direction cosines in terms of Euler angles are obtained. Three rotations are defined. The first is θ_z which is taken with respect to the original material axis x_3. After that rotation is carried out, a rotation about the new x_1 axis is defined as θ_x. Finally, a rotation is taken about the new x_2-axis and defined as θ_y. The reader should not be confused by the subscripts of these angles. They are not taken with respect to the crack axes. With these angles, the direction cosines are found as

$$\begin{aligned} t_{11} &= \cos\theta_z \cos\theta_y - \sin\theta_z \sin\theta_x \sin\theta_y, \\ t_{12} &= -\sin\theta_z \cos\theta_x, \\ t_{13} &= \cos\theta_z \sin\theta_y + \sin\theta_z \sin\theta_x \cos\theta_y, \\ t_{21} &= \sin\theta_z \cos\theta_y + \cos\theta_z \sin\theta_x \sin\theta_y, \\ t_{22} &= \cos\theta_z \cos\theta_x, \\ t_{23} &= \sin\theta_z \sin\theta_y - \cos\theta_z \sin\theta_x \cos\theta_y, \\ t_{31} &= -\cos\theta_x \sin\theta_y, \\ t_{32} &= \sin\theta_x, \\ t_{33} &= \cos\theta_x \cos\theta_y. \end{aligned} \tag{45}$$

If the transformation is carried out as done by the elasticity community, some of the signs in t_{ij} change and the Euler angles are the negative of those defined above. But the same matrix of direction cosines is found.

Following Ting [13], pp. 54–55, the components of the 3×3 matrix of direction cosines may be used to formulate two 6×6 matrices for rotating the material stiffness and compliance matrices. These matrices are given as

$$\mathbf{R}_s = \begin{bmatrix} t_{11}^2 & t_{12}^2 & t_{13}^2 & t_{12}t_{13} & t_{13}t_{11} & t_{11}t_{12} \\ t_{21}^2 & t_{22}^2 & t_{23}^2 & t_{22}t_{23} & t_{23}t_{21} & t_{21}t_{22} \\ t_{31}^2 & t_{32}^2 & t_{33}^2 & t_{32}t_{33} & t_{33}t_{31} & t_{31}t_{32} \\ 2t_{21}t_{31} & 2t_{22}t_{32} & 2t_{23}t_{33} & t_{22}t_{33} + t_{23}t_{32} & t_{23}t_{31} + t_{21}t_{33} & t_{21}t_{32} + t_{22}t_{31} \\ 2t_{31}t_{11} & 2t_{32}t_{12} & 2t_{33}t_{13} & t_{32}t_{13} + t_{33}t_{12} & t_{33}t_{11} + t_{31}t_{13} & t_{31}t_{12} + t_{32}t_{11} \\ 2t_{11}t_{21} & 2t_{12}t_{22} & 2t_{13}t_{23} & t_{12}t_{23} + t_{13}t_{22} & t_{13}t_{21} + t_{11}t_{23} & t_{11}t_{22} + t_{12}t_{21} \end{bmatrix} \tag{46}$$

Please cite this article as: Leslie Banks-Sills et al., Methods for calculating stress intensity factors in anisotropic ..., Engineering Fracture Mechanics (2006), doi:10.1016/j.engfracmech.2006.07.005

and

$$\mathbf{R}_{\mathrm{c}} = \begin{bmatrix} t_{11}^2 & t_{12}^2 & t_{13}^2 & 2t_{12}t_{13} & 2t_{13}t_{11} & 2t_{11}t_{12} \\ t_{21}^2 & t_{22}^2 & t_{23}^2 & 2t_{22}t_{23} & 2t_{23}t_{21} & 2t_{21}t_{22} \\ t_{31}^2 & t_{32}^2 & t_{33}^2 & 2t_{32}t_{33} & 2t_{33}t_{31} & 2t_{31}t_{32} \\ t_{21}t_{31} & t_{22}t_{32} & t_{23}t_{33} & t_{22}t_{33} + t_{23}t_{32} & t_{23}t_{31} + t_{21}t_{33} & t_{21}t_{32} + t_{22}t_{31} \\ t_{31}t_{11} & t_{32}t_{12} & t_{33}t_{13} & t_{32}t_{13} + t_{33}t_{12} & t_{33}t_{11} + t_{31}t_{13} & t_{31}t_{12} + t_{32}t_{11} \\ t_{11}t_{21} & t_{12}t_{22} & t_{13}t_{23} & t_{12}t_{23} + t_{13}t_{22} & t_{13}t_{21} + t_{11}t_{23} & t_{11}t_{22} + t_{12}t_{21} \end{bmatrix}. \tag{47}$$

With respect to the global coordinate system, the rotated material matrices are

$$\mathbf{C}^* = \mathbf{R}_{\mathrm{c}}\widehat{\mathbf{C}}\mathbf{R}_{\mathrm{c}}^{\mathrm{T}}, \tag{48}$$

$$\mathbf{S}^* = \mathbf{R}_{\mathrm{s}}\widehat{\mathbf{S}}\mathbf{R}_{\mathrm{s}}^{\mathrm{T}}. \tag{49}$$

After the finite element results are obtained, the M-integral is implemented in the local, crack tip coordinate system (x, y, z). Once again the compliance and stiffness matrices are rotated. This time from the global finite element coordinate system to the crack tip coordinates. The matrix of direction cosines is denoted as $\mathbf{t}'$. The transformation of the material matrices is given by

$$\mathbf{C} = \mathbf{R}'_{\mathrm{c}}\mathbf{C}^*\mathbf{R}'^{\mathrm{T}}_{\mathrm{c}}, \tag{50}$$

$$\mathbf{S} = \mathbf{R}'_{\mathrm{s}}\mathbf{S}^*\mathbf{R}'^{\mathrm{T}}_{\mathrm{s}}. \tag{51}$$

The components of $\mathbf{R}'_{\mathrm{c}}$ and $\mathbf{R}'_{\mathrm{s}}$ are the same as that of $\mathbf{R}_{\mathrm{c}}$ and $\mathbf{R}_{\mathrm{s}}$, with the components of $\mathbf{t}$ replaced by those of $\mathbf{t}'$ where the latter 3×3 matrix contains the directions cosines between the local crack tip coordinate system and the global finite element coordinates.

References

[1] Banks-Sills L, Hershkovitz I, Wawrzynek PA, Eliasi R, Ingraffea AR. Methods for calculating stress intensity factors in anisotropic materials: Part I—$z = 0$ is a symmetric plane. Engng Fract Mech 2005;72(15):2328–58.
[2] Hoenig A. Near-tip behavior of a crack in a plane anisotropic elastic body. Engng Fract Mech 1982;16(3):393–403.
[3] Lekhnitskii SG. Theory of elasticity of an anisotropic body. San Francisco: Holden-Day, 1950, in Russian, 1963, in English, translated by Fern P.
[4] Yau JF, Wang SS, Corten HT. A mixed-mode crack analysis of isotropic solids using conservation laws of elasticity. J Appl Mech 1980;47(2):335–41.
[5] Wang SS, Yau JF, Corten HT. A mixed-mode crack analysis of rectilinear anisotropic solids using conservation laws of elasticity. Int J Fract 1980;16(3):247–59.
[6] Shih CF, Moran B, Nakamura T. Energy release rate along a three-dimensional crack front in a thermally stressed body. Int J Fract 1986;30(2):79–102.
[7] Freed Y, Banks-Sills L. A through interface crack between a ±45° transversely isotropic pair of materials. Int J Fract 2005;133(1):1–44.
[8] Banks-Sills L, Travitzky N, Ashkenazi D, Eliasi R. A methodology for measuring interface fracture toughness of composite materials. Int J Fract 1999;99(3):143–61.
[9] Swanson G, Arakere NK. Effect of crystal orientation on the analysis of single-crystal, nickel-based turbine blade superalloys. NASA Technical Report, NASA/TP-2000-210074, 2000.
[10] FRANC3D, Cornell Fracture Group. Available from: www.cfg.cornell.edu 2005.
[11] ANSYS, Release 8.1, Ansys, Inc., Canonsburg, Pennsylvania, 2004.
[12] Fung YC. A first course in continuum mechanics. New Jersey: Prentice-Hall; 1969.
[13] Ting TCT. Anisotropic elasticity—theory and applications. Oxford: Oxford University Press; 1996.